Biomedical engineering

Interpreting magnetic fields of the brain: minimum norm estimates

M. S. Hämäläinen **R. J. Ilmoniemi**

Low Temperature Laboratory, Helsinki University of Technology, 02150 Espoo, Finland

Abstract—*The authors have applied estimation theory to the problem of determining primary current distributions from measured neuromagnetic fields. In this procedure, essentially nothing is assumed about the source currents, except that they are spatially restricted to a certain region. Simulation experiments show that the results can describe the structure of the current flow fairly well. By increasing the number of measurements, the estimate can be made more localised. The current distributions may be also used as an interpolation and an extrapolation for the measured field patterns.*

Keywords—*Inverse problem, Minimum-norm estimate, Neuromagnetism*

Med. & Biol. Eng. & Comput., 1994, 32, 35–42

1 Introduction

IN NEUROMAGNETISM, information about electrical currents in the brain is obtained by measuring the magnetic-flux density at several points outside the head (HÄMÄLÄINEN *et al.*, 1993). Like many other inverse problems, that of neuromagnetism is non-unique; there are infinite current distributions that can explain the measurements.

The most common method to deal with the inverse problem is to characterise the current distribution with a small number of parameters. However, it is often difficult to find a source model that is simultaneously restrictive enough to make the problem unique and also capable of describing the essential features of the current distribution. A widely used model, suitable for interpreting the simplest neuromagnetic field patterns, is the current dipole (WILLIAMSON and KAUFMAN, 1981).

Application of the dipole model in locating brain activity implicitly presupposes that the source current is localised in one small area (or in several separate sites in multi-dipole models). Misleading results can be obtained if these assumptions are not valid.

In this paper, we present minumum-norm estimates (MNEs) for the source-current distribution. These are the best estimates for the current when minimal *a priori* information about the source is available. When no assumptions about discrete current elements are made, the estimates turn out to be continuous current distributions. This approach was introduced in a technical report (HÄMÄLÄINEN and ILMONIEMI, 1984) and at a conference (ILMONIEMI *et al.*, 1985); it has subsequently been discussed by several authors (KULLMANN *et al.*, 1989; CLARKE *et al.*, 1989; CROWLEY *et al.*, 1989; IOANNIDES *et al.*, 1990; DALLAS, 1985; SINGH *et al.*, 1984; JEFFS *et al.*, 1987; SMITH *et al.*, 1990). Although our specific examples deal with the interpretation of neuromagnetic data, an identical treatment is also suitable for electro-encephalography (EEG). In a companion paper (NENONEN *et al.*, 1994), the method is applied to the inverse problem in electro- and magneto-cardiography (ECG and MCG).

As a solution to the difficulty encountered in interpolating or extrapolating magnetic-field or electric-potential maps, we propose the use of minimum-norm estimates. From the original data, the MNE is computed first; the magnetic or electric field at desired points on a given surface can then be calculated directly from the MNE.

Correspondence should be addressed to Matti Hämäläinen

First received 3 June 1992 and in final form 13 January 1993

2 Methods

We shall analyse the inverse problem of magneto-encephalography, proposing that a linear combination of magnetometer lead fields should be used as an estimate for the primary-current distribution in the brain. The lead field is a vector field that describes the sensitivity pattern of a magnetometer to the primary current.

2.1 *Definition of the lead field*

Let us denote the primary-current density with $\boldsymbol{J}^p$: $\boldsymbol{J}^p(\boldsymbol{r}) = \boldsymbol{J}_{tot}(\boldsymbol{r}) - \sigma(\boldsymbol{r})\boldsymbol{E}(\boldsymbol{r})$, where $\boldsymbol{r}$ is the position vector, $\boldsymbol{J}_{tot}$ is the total current density, σ is the conductivity, and $\boldsymbol{E}$ is the electric field. $\boldsymbol{J}^p$ is the result of a change of other types of energy into electrical form: it provides the battery of the circuit (PLONSEY, 1969), driving volume currents ($\sigma\boldsymbol{E}$) in the conductor. We consider σ, $\boldsymbol{J}^p$, and $\boldsymbol{E}$ on a macroscopic scale, so that these quantities are the average or effective values over a volume of about 1 mm^3.

The output of a magnetometer B_i is linearly related to the primary-current distribution. We can therefore find a vector field $\boldsymbol{L}_i(\boldsymbol{r})$ satisfying

$$B_i = \int \boldsymbol{L}_i(\boldsymbol{r}) \cdot \boldsymbol{J}^p(\boldsymbol{r}) dv. \quad (1)$$

$L_i(r)$ is called the lead field; it describes the sensitivity distribution of the ith magnetometer (MALMIVUO, 1976; TRIPP, 1983). In addition to the coil configuration of the magnetometer, the lead field depends on the conductivity $\sigma = \sigma(r)$. Although the use of realistically shaped conductor models is emerging (HÄMÄLÄINEN, 1989), in this paper, we assume a spherically symmetric or horizontally layered conductor (CUFFIN and COHEN, 1977); our results are directly applicable to any linear conductor model (NENONEN *et al.*, 1994).

The lead field, as defined by eqn. 1, can be computed, provided that it is possible to calculate the magnetic field $B_i = B_i(Q, r')$, resulting from an arbitrary current dipole Q at r'. This requires knowledge of the conductivity distribution $\sigma(r)$, so that the effect of volume currents can be properly taken into account. For Q at r', $J^p(r) = Q\delta(r - r')$, where $\delta(r)$ is the Dirac delta function. Inserting this dipolar primary-current distribution into eqn. 1, we obtain

$$B_i(Q, r') = L_i(r') \cdot Q \tag{2}$$

With eqn. 2 all three components of $L_i(r')$ can be found for any r'.

2.2 *Minimum-norm estimate for a current distribution*

In the following, primary-current distributions (in general, continuous) are considered as elements of a function space $\mathcal{F}$ that contains all square-integrable current distributions, confined to a known set of points G inside a conductor; $\mathcal{F}$ is called the current space. The set G, in which J^p is confined, may be a curve, a surface or a volume region, or a combination of discrete points, depending on the nature of the problem. When we refer to current distributions as elements of the current space, we use capital letters. The inner product of two currents $J_1 \in \mathcal{F}$ and $J_2 \in \mathcal{F}$ is defined by

$$\langle J_1, J_2 \rangle = \int_G J_1(r) \cdot J_2(r) dG \tag{3}$$

The overall amplitude or 'length' of a current distribution is described by its norm:

$$\|J_k\|^2 = \langle J_k, J_k \rangle = \int_G |J_k^p(r)|^2 \, dG \tag{4}$$

From eqn. 1, it is evident that measurements $B_i = \langle L_i, J^p \rangle$, $i = 1, \ldots, M$, only yield information about primary currents lying in the subspace $\mathcal{F}'$ of the current space $\mathcal{F}$. This subspace is spanned by the lead fields; $\mathcal{F}' = \text{span}(L_1, \ldots, L_M)$. The idea of an MNE is that we search for an estimate J^* for J^p that is confined to $\mathcal{F}'$. J^* will then be a linear combination of the lead fields:

$$J^* = \sum_{j=1}^{M} w_j L_j \tag{5}$$

where w_j are scalars to be determined from the measurements. Requiring J^* to reproduce the measured signals $\langle L_i, J^* \rangle = B_i = \langle L_i, J^p \rangle$, we obtain a set of linear equations $b = \Gamma w$, where $b = (B_1, \ldots, B_M)^T$, $w = (w_1, \ldots, w_M)^T$, and Γ is an $M \times M$ matrix containing the inner products of the lead fields $\Gamma_{ij} = \langle L_i, L_j \rangle$. With this notation, eqn. 5 can be compactly written as $J^* = w^T L$, where $L = (L_1, \ldots, L_M)^T$.

The term minimum-norm estimate derives from the fact that, in the sense of the norm defined by eqn. 4, J^* is the shortest current vector capable of explaining the measured signals. The non-uniqueness of the inverse problem is manifested by the fact that the actual current distribution producing b may be any current of the form $J = J^* + J_\perp$, where $J_\perp$ satisfies $\langle J_\perp, L_i \rangle = 0$, $i = 1, \ldots, M$. In other words, any primary-current distribution (together with volume currents) to which the measuring instrument is not sensitive may be added to the solution.

2.3 *Regularisation*

If the lead fields are linearly independent, which is generally the case when the measurements are made at different locations, the inner product matrix Γ is non-singular and

$$w = \Gamma^{-1} b \tag{6}$$

However, in practice, the L_is may be nearly linearly dependent. Thus, Γ can possess some very small eigenvalues, which leads to large errors in the computation of w.

To avoid this numerical instability, the solution must be regularised. This means that directions in $\mathcal{F}'$ with poor coupling to the sensors must be suppressed. Let $\Gamma = V \Lambda V^T$, with $V^T V = I$ and $\Lambda = \text{diag}\ (\lambda_1, \ldots, \lambda_M)$, where $\lambda_1 > \lambda_2 > \ldots \lambda_M > 0$ are the eigenvalues of Γ. Then, $\Gamma^{-1} = V \Lambda^{-1} V^T$. Regularisation may be carried out by replacing Λ^{-1} by $\tilde{\Lambda}^{-1} = \text{diag}(\lambda_1^{-1}, \ldots, \lambda_K^{-1}, 0, \ldots, 0)$ to obtain a regularised inverse $\tilde{\Gamma}^{-1} = V \tilde{\Lambda}^{-1} V^T$. The cut-off value $K \leqslant M$ is selected so that the regularised MNE does not contain excessive contributions from noise. The minimum-norm estimate does not then exactly reproduce the measured signals, but the misfit $b - \tilde{b}$, where $\tilde{b} = \Gamma \tilde{\omega} = \Gamma \tilde{\Gamma}^{-1} b$, is in accordance with measurement errors, (SARVAS, 1987). In terms of current distributions, regularisation means that those eigenleads that correspond to small eigenvalues, and thus are hard to measure with sufficient signal-to-noise ratio, are ignored. The regularised minimum-norm solution is

$$\tilde{J}^* = (\tilde{\Gamma}^{-1} b)^T L \tag{7}$$

In the remainder of this paper, we always apply regularisation and denote the estimates simply by J^* instead of $\tilde{J}^*$.

2.4 *Isocontour maps*

A conventional way to present the spatial pattern of MEG data is to display isocontour plots at selected time instants. This approach is straightforward as long as all measurements are uniform in the sense that the same field component, usually the radial component B_r, is measured. However, with wide-area multichannel magnetometers, it can be difficult or even impossible to align all channels in the radial direction. Therefore the isocontour plots may be misleading because some channels are tilted or further away from the head than others.

There are also planar multichannel magnetometers (AHONEN *et al.*, 1992; KAJOLA *et al.*, 1989) that are sensitive to off-diagonal derivatives of the magnetic field. It would be useful, for the purpose of data comparison, to show results obtained with planar gradiometers as isocontour plots as well. For this we need an estimate of B_r from field derivatives. As different laboratories use magnetometers with different coil configurations, it would be desirable to establish a common form of data representation. Such standardisation would facilitate the comparison of measurements between laboratories and also within a laboratory, and between different sessions on an individual subject.

MNEs are convenient and reliable for neuromagnetic data interpolation and extrapolation; from the MNE, all

components of the magnetic field at any desired location can be directly computed (ILMONIEMI and NUMMINEN, 1992). Suppose we want to obtain field values in some target grid. Let the lead fields of the virtual magnetometers be $L'_1, \ldots, L'_{M'}$ and the corresponding virtual measurements be $b' = (b'_1, \ldots, b'_{M'})^T$. By combining the definition of the lead field $b'_k = \langle L'_k, J^* \rangle$ with eqn. 5, we obtain

$$b'_k = \sum_{j=1}^{M} w_j \langle L_j, L'_k \rangle \tag{8}$$

or

$$b' = \Gamma' w \tag{9}$$

where $\Gamma'_{jk} = \langle L'_j, L_k \rangle$. With the expression for w from eqn. 6, we finally obtain the interpolation or extrapolation

$$b' = \Gamma' \Gamma^{-1} b \tag{10}$$

Of course, if Γ possesses small eigenvalues, the regularised inverse must be used, but in this case, as the measured field pattern is to be displayed, a milder regularisation is probably preferable.

Our MNE-based interpolation method automatically takes into account the mechanism, described by Maxwell equations, that generates the magnetic field. The result is free of artefacts and smooth in the way required by the electromagnetic theory, which is not the case with the purely mathematical interpolation methods applied so far in this context. Other source models, e.g. a collection of current dipoles, could, in principle, also be used in the interpolation. However, finding the best source model would then require a least-squares fit, and furthermore, restricting assumptions about the source would be inevitable.

2.5 *Utilisation of potential measurements*

Far older than biomagnetism is the study of human body functions by means of surface potential measurements. The changes in the electrical potential on the scalp, as obtained by EEG, are due to the same source currents that are responsible for the magnetic field outside the head. However, as MEG is insensitive to the radial current sources detectable with potential measurements, it is, at least in principle, possible to widen the scope of the source-current estimates by combining EEG and MEG data.

Let V_i be the voltage between two electrodes. The lead field $\boldsymbol{L}_i^E(\boldsymbol{r})$ of the electrode pair can be defined analogously with eqn. 1:

$$V_i = \int \boldsymbol{L}_i^E(\boldsymbol{r}) \cdot \boldsymbol{J}^p(\boldsymbol{r}) dv \tag{11}$$

We now assume magnetic-field measurements $b = (B_1, \ldots, B_M)^T$ and voltage measurements $v = (V_1, \ldots, V_N)^T$. The MNE then lies in the subspace spanned by the magnetic lead fields $L_1, \ldots, L_M$ and the electric lead fields $L_1^E, \ldots, L_N^E$, and eqn. 5 becomes

$$J^* = \sum_{j=1}^{M} w_j L_j + \sum_{k=1}^{N} w_k^E L_k^E \tag{12}$$

The weights w_j and w_k^E are now determined from the equations

$$\begin{pmatrix} b \\ v \end{pmatrix} = \begin{pmatrix} \Gamma^{bb} & \Gamma^{bv} \\ \Gamma^{vb} & \Gamma^{vv} \end{pmatrix} \begin{pmatrix} w \\ w^E \end{pmatrix} \tag{13}$$

where $\Gamma_{ij}^{bb} = \langle L_i, L_j \rangle$, $\Gamma_{ij}^{vv} = \langle L_i^E, L_j^E \rangle$, $\Gamma_{ij}^{bv} = \langle L_i, L_j^E \rangle$ and $\Gamma^{vb} = (\Gamma^{bv})^T$.

As MEG and EEG are formally in an identical role, their separate treatment is unnecessary. However, for certain distributions of the conductivity and the set of points that define the current space, the cross terms Γ^{bv} and Γ^{vb} vanish; in such cases, MEG and EEG provide completely independent information. Spherical symmetry is one such situation. In the general case, EEG and MEG bring data that are partially redundant. Voltage measurements provide signals from radial source currents, which make only a small contribution to the magnetic field outside the head (in the spherical model, zero contribution). Tangential source currents affect both the voltage and the magnetic field. By using MEG and EEG simultaneously, a better source-current estimate can be obtained than by either method alone (NENONEN *et al.*, 1994).

3 Results

We investigated the properties of MNEs with simulations and applied them to brain measurements.

3.1 *Simulations without noise*

We shall describe two series of simulation experiments. In the first set, the area covered by the magnetometers was kept fixed but the number of channels was varied. In the second set, the number was fixed but the mutual distances between channels changed.

The conductivity geometry was assumed to be such that no volume currents had to be taken into account explicitly. This assumption is valid, for example, in the case of a conducting half-space, where σ is a function of z only. Our choice of conductivity distribution is for convenience only; currents in more complicated geometries would not essentially change the results, as long as the effect of $\sigma(\boldsymbol{r})$ on the lead fields is properly calculated to satisfy eqn. 1. Point magnetometers, measuring the z-component of the magnetic field, were assumed in the simulations. The integration area G (eqn. 3) was chosen to be part of a plane parallel to the xy-plane. The restriction means that the source current is assumed to be confined to this area.

Once the arrangement of the sensors had been chosen, the signal in each magnetometer was calculated from test-current dipoles. Normally distributed random numbers, representing a specified level of white noise, could be added to each signal.

The estimates, which are continuous primary-current distributions, are visualised with arrow maps, where each arrow points in the direction of the estimated current density at the centre of the arrow. Its length is proportional to the current density at that point.

The MNE can be calculated for any number and arrangement of sensors. In particular, it is not necessary to cover the whole source area. However, the resolution is degraded if the number of channels is reduced or if the magnetometers do not adequately cover the field pattern.

In the first set of experiments, 4, 9, 16, 25, and 36 point magnetometers were placed in a planar square lattice to cover an area of $80 \times 80\ \text{mm}^2$ in the $z = 30$ mm plane. Therefore the lattice constants, i.e. distances between neighbouring channels, were 80, 40, 26·6, 20 and 16 mm, respectively. The source current was assumed to be confined to a square of $200 \times 200\ \text{mm}^2$ in the xy-plane, 30 mm from the magnetometer plane. The test source was a single-current dipole.

Fig. 1 shows the results of experiments with 16 and 36 magnetometers. The current estimate is more tightly localised when there are 36 magnetometers than when there are only 16 magnetometers.

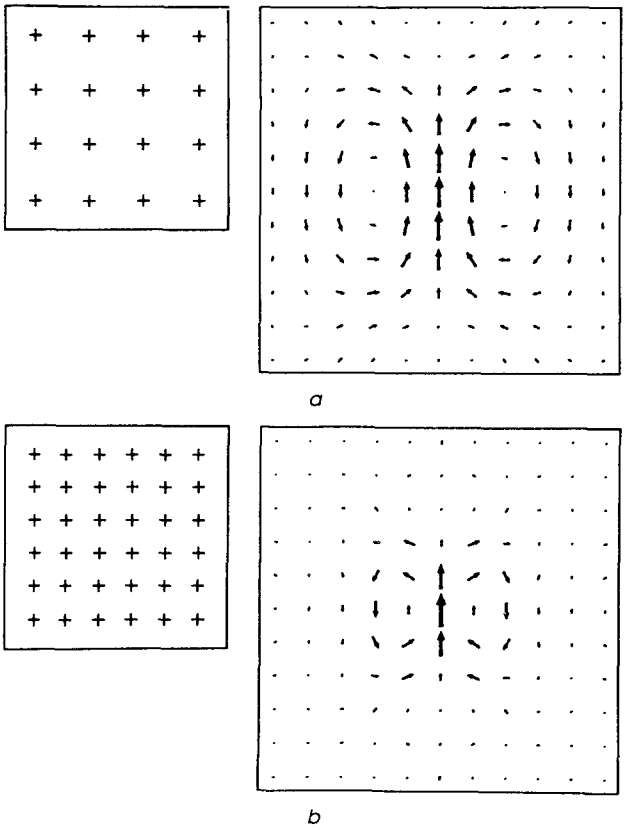

Fig. 1 *Effect of the number of magnetometers on the current estimate in the case of a dipolar test source. The estimates are continuous current distributions, but here they are displayed as arrow maps, centred at the location of the test source. Each arrow denotes the estimated primary-current density at its centre. The lattice constant in the arrow maps is 10 mm. The positions of the magnetometers relative to each other are indicated by the crosses in the panels to the left of the current estimates. The magnetometer grids are shown in the same scale as the arrow maps. In the simulations, the measurement grid was 30 mm directly above the test source, which was a vertically-oriented current dipole. (a) 16 magnetometers, (b) 36 magnetometers*

The second set of experiments used 25 point magnetometers in a square lattice 30 mm from the source-current plane. The neighbouring magnetometers were 10, 20 and 30 mm from each other. The integration area and the test current were the same as in the first simulations. The results were similar; the estimates were most precisely localised when the magnetometers were close to each other. If the dipole was outside the area covered by the magnetometers, the estimate became distorted. However, even then, an experimenter could form an idea about the location of the source, being able to move the magnetometer array to cover the appropriate area.

3.2 *Effect of noise*

To simulate a realistic measurement situation, we assumed a coil configuration identical to that in our 24-channel system (KAJOLA *et al.*, 1989). Its planar gradiometers sense the off-diagonal derivatives $\partial B_z/\partial x$ and $\partial B_z/\partial y$ at 12 locations simultaneously; B_z is the field component perpendicular to the curved bottom of the dewar. The array covers a spherical cap with a diameter of 125 mm (Fig. 2).

The source dipoles were lying on a spherical surface of 90 mm radius. The centre of this surface coincides with the centre of curvature of the gradiometer coils.

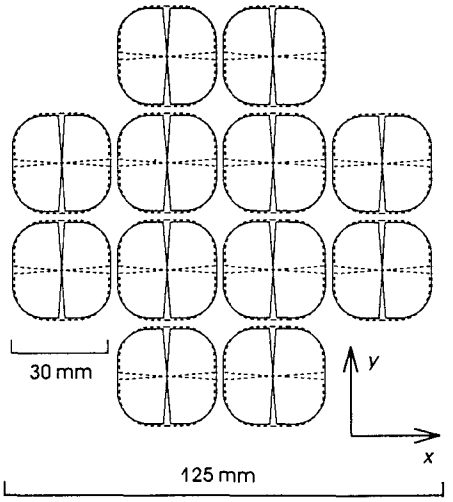

Fig. 2 *Coil configuration of our 24-channel gradiometer, projected to a plane. Each of the 12 units consists of two orthogonal figure-of-eight loops. Those illustrated with solid lines sense the derivative $\partial B_z/\partial x$, and the loops shown with dashed lines measure $\partial B_z/\partial y$. Here B_z denotes the field component normal to the dewar bottom at each sensor-pair location*

Uncorrelated Gaussian noise of different amplitudes was added to the test signals computed from the dipole sets. In the examples shown, an RMS noise of 12 fT cm^{-1} was assumed. This is about twice the actual noise level of our instrument, thus also accounting for some additional noise from random brain activity.

The regularisation technique described in Section 2.3 was applied to suppress the effect of noise on the current estimates. It was found that the selection of the cut-off point K, needed to compute the current estimate according to eqn. 7, was not critical. Judging from the behaviour of the current estimates and the scaled norm of the misfit to the experimental data

$$g = \sqrt{\frac{1}{M}(b - \tilde{b})^T(b - \tilde{b})} \tag{14}$$

where $M = 24$ is the number of measurements, it was found that any value $17 \leqslant K \leqslant 22$ gives satisfactory results. Fewer eigenleads resulted in missing the details of the current distribution, whereas larger values for K exhibited spurious noise currents. Here we show results for $K = 21$. The selection of proper regularisation could be automated with cross-validation techniques (GOLUB *et al.*, 1979).

The current estimates are depicted in Fig. 3. We note that essential features of the test-current configurations can be resolved by the estimates. Here, because the test sources consist of current dipoles, the maxima of the estimates are approximately at the sites of the test dipoles. If the current dipole nature of the sources were not assumed prior to the measurement, the location of activity should be judged directly from the current estimates, instead of using the sites of equivalent current dipoles. It should be emphasised that no assumption about the number or nature of sources is needed in this procedure. The spatial resolution is poor, but there is no way to do better without additional constraints on the solution.

3.3 *Isocontour maps*

As an example of the MNE data interpolation method, described in Section 2.4, we show how the effect of tilted magnetometer orientations is eliminated.

This simulation assumed a multichannel magnetometer sensing B_r, the component of the magnetic field

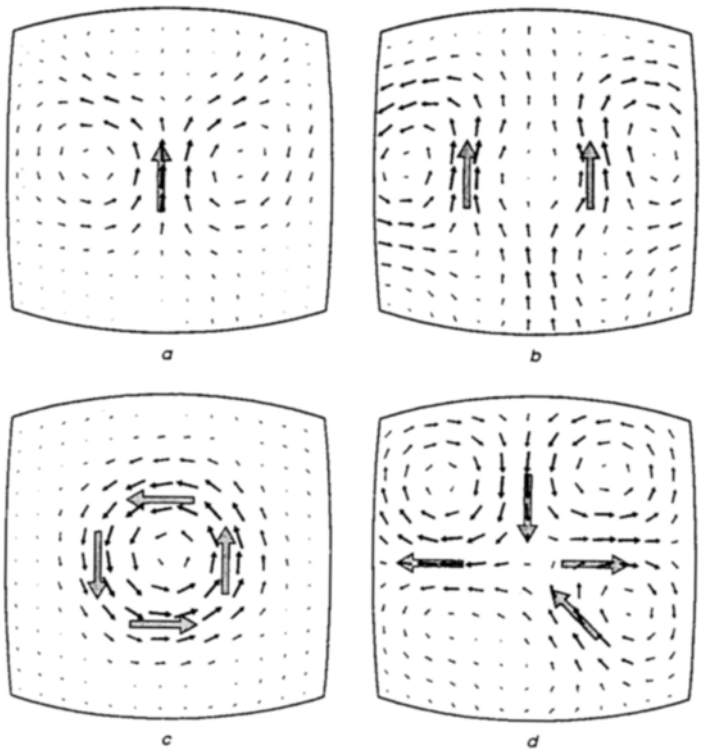

Fig. 3 *Estimates from signals originating from various source configurations. The lattice constant in the arrow maps is 6.3 mm, corresponding to an angular step of 4° on the 90 mm surface. The assumed test dipoles (Q = 10 nAm) are depicted by the large arrows. For the two-dipole case (b), an additional activation area, caused by the simulated noise in the measurement signals, appears in the bottom part of the Figure. For other sets of noisy signals with the same sources, the additional activity was smaller or appeared elsewhere in the source area*

perpendicular to a curved surface with 125 mm radius. The device was assumed to have 25 channels, evenly distributed in a close-to-square lattice of 125 mm diameter.

Two measurements were simulated; one with all magnetometers oriented normal to the spherical surface of the head, and another with the whole array tilted by 12°. The distance of the magnetometers from the surface of the head was 15 mm in the untilted orientation. The current source was a dipole (Q = 10 nAm) at a depth of 15 mm from the surface of the head.

Three field maps were constructed; the first was constructed from the untilted measurement with a standard interpolation method (McLain, 1974), the second from the tilted measurement with the same procedure, and the third from the tilted measurement using the new MNE interpolation method (Fig. 4). With the tilted array, MNE interpolation produced a result that is almost identical to that from the untilted measurement, whereas conventional interpolation gave a strong asymmetry and a slight shift of the zero-line. It appears that MNE interpolation offers a possibility to compare field maps obtained with different devices or with different placements of one device. This may be essential for the comparison of data between laboratories.

4 Analysing evoked responses

The estimation procedure described above was applied to visually evoked magnetic signals.We measured the field pattern as a function of time over the occipital part of the head, during and after the presentation of stimuli to the subject (Ahlfors *et al.*, 1992). These are checkerboard patterns modified so that the check size increases as a function of distance from the centre of the visual field, in order to compensate for the lower acuity in the periphery (Fig. 5*b*). Stimuli were presented in one octant of the visual field at a time, either in the foveal or the parafoveal area. The subject was instructed to look at a fixation point on a computer screen. The different stimuli were then shown for a period of about 250 ms in random order, so that the time between their successive appearances varied randomly between 850 and 1250 ms. Each group of six stimulus presentations was separated from the next group by an interval of about 5 s, during which the subject could relax.

Fig. 5*a* shows the averaged signals from the 24 magnetometer channels, reflecting the electrical activity of the visual cortex as a consequence of the parafoveal stimulus pattern in octant 7. The first major deflection occurs at about 70 ms after the stimulus. At present, we do not know how many simultaneous sources produce the

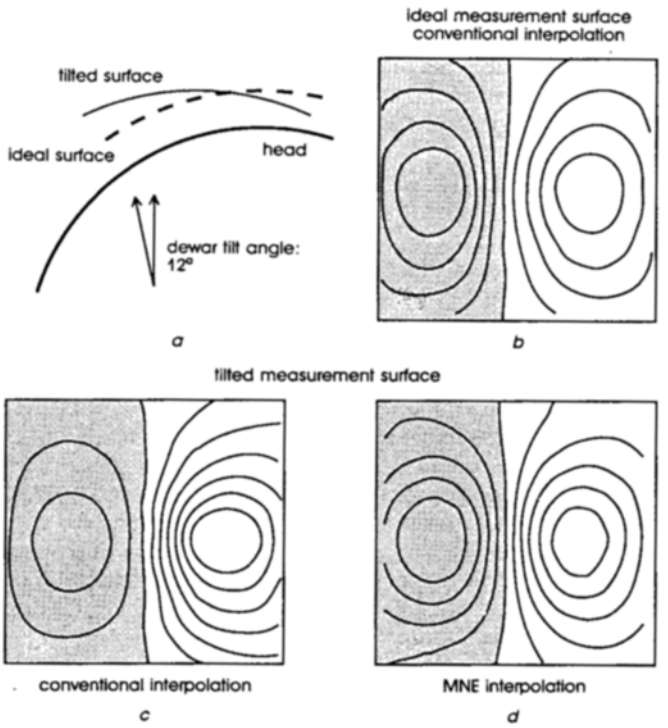

Fig. 4 *Example of MNE interpolation: (a) tilted and ideal magnetometer surfaces: (b) conventional interpolation from a measurement on the ideal (untilted) surface; (c) and (d) conventional and MNE interpolation from the tilted surface. Notice the large and potentially misleading asymmetry in (c)*

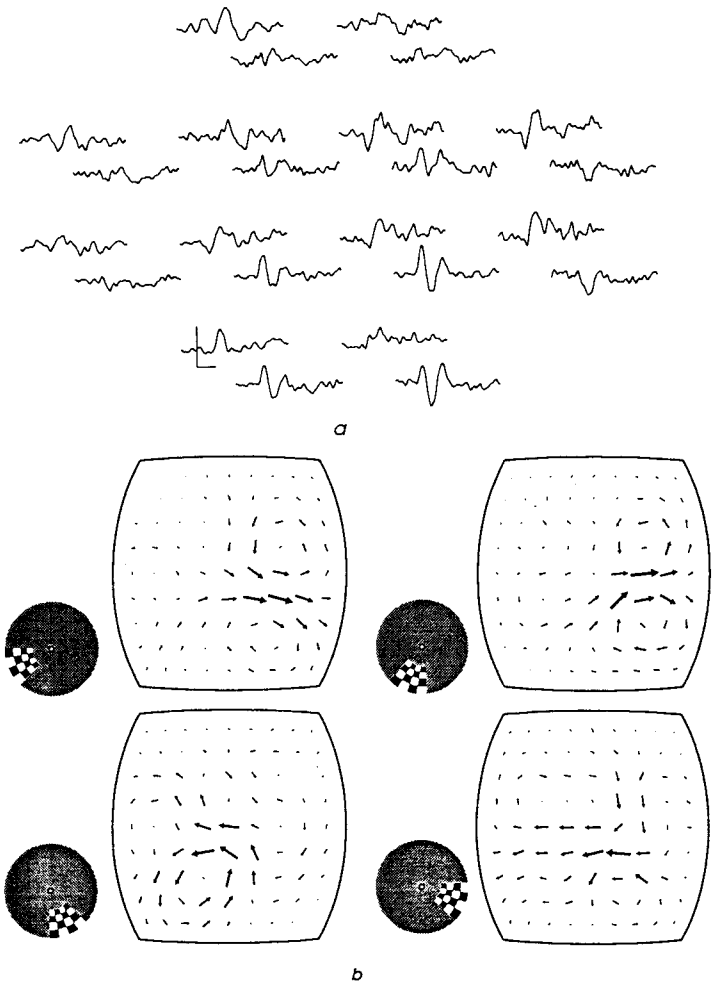

Fig. 5 *Visual experiment (AHLFORS et al., 1992): (a) averaged magnetic field as a result of the presentation of a parafoveal pattern in octant 7, from all 24 channels, as a function of time. The horizontal line segment below one of the traces corresponds to the first 100 ms after the stimulus onset. The recording passband of 0.05–100 Hz was reduced to 1–35 Hz with a software filter; (b) MNEs for parafoveal stimuli, shown to the left of each current estimate. The MNEs have been calculated using the convenient assumption that the primary current lies on a spherical surface placed 10 mm below the scalp; therefore no depth information is obtained. However, it is evident from these MNEs that for left visual-field stimuli, the primary current is on the right, and that for right visual-field stimuli, the current is on the left. The area shown has an angular extent of 40°; the centre of the depicted area is 30 mm above inion towards vertex.*

magnetic field at different times. However, we may form a rough idea of the cerebral locations that are involved by calculating the minimum-norm estimates of the source-current distribution. Fig. 5*b* shows these during the 70 ms deflection of the magnetic field, evoked by parafoveal patterns presented in visual field octants 5–8. It is apparent that the activity is on the side of the brain opposite to the stimulus.

5 Discussion

We have applied estimation theory to the problem of determining primary-current distributions from measured magnetic fields. In this procedure, essentially nothing is assumed about the source currents except that they are confined to a certain region, for example the brain. A known conductivity distribution is assumed, however, so that the effect of volume currents can be properly taken into account. In the sense of the Euclidean norm, our estimate is the shortest vector in the source-current space that can explain the measurements. The error is orthogonal to the subspace defined by the lead fields. Therefore the only way to improve the estimate is to provide some additional information. An example is the assumption of the dipole model when interpreting evoked responses.

It would be desirable to improve the MNEs by finding ways to inject some *a priori* knowledge or assumptions of the experimenter (SMITH *et al.*, 1990). We emphasise that we should make only such restrictions as are justified by prior knowledge. For example, if magnetic-resonance images are available, it is possible to find the shape of the cortex and accordingly restrict the integration area.

We feel that minimum-norm estimates are better than magnetic isocontour maps in expressing the results of MEG measurements. The magnetic field is only a medium that conveys information from the brain. As we are primarily interested in the distribution of activity in the brain, we should express our results in the form of current-source distributions. In the transformation of data into minimum-norm estimates, practically no information is lost; the results are only transformed into another form. Even when the dipole model is applied, the minimum-norm estimate can be the starting point. For example, it is possible to guess from the maxima of Fig. 3 the location of some of the current dipoles.

The simulation experiments show that our estimates can describe the structure of the current distribution fairly well. By increasing the number of magnetometers, the estimate can be made more localised.

Acknowledgments—The authors would like to thank Olli V. Lounasmaa for support and constructive criticism; Seppo Ahlfors for the preparation of the visual data; Riitta Hari, Jukka Knuutila, Matti Kajola, Mikko Sams, Jukka Sarvas and Michael Scherg for discussions and comments on the manuscript.

This work was supported by the Academy of Finland, the Finnish National Fund for Research and Development (SITRA) and Instrumentarium Corp.

References

AHLFORS, S. P., ILMONIEMI, R. J. and HÄMÄLÄINEN, M. S. (1992): 'Estimates of visually evoked cortical currents,' *Electroenceph. Clin. Neurophysiol.*, **82**, pp. 225–236

AHONEN, A. I., HÄMÄLÄINEN, M. S., KAJOLA, M. J., KNUUTILA, J. E. T., LAINE, P. P., LOUNASMAA, O. V., SIMOLA, J. T., TESCHE, C. D. and VILKMAN, V. A. (1992): 'A 122-channel magnetometer covering the whole head' *in* DITTMAR, A. and FROMENT, J. C.

(Eds.): Proc. Satellite Symp. on Neuroscience and Technology, 14th Annual Conf. of the IEEE Engineering in Medicine and Biology Society (IEEE Engineering in Medicine and Biology Society, Lyon) pp. 16–20
CLARKE, C. J. S., IOANNIDES, A. A., and BOLTON, J. P. R. (1989): 'Localised and distributed source solutions for the biomagnetic inverse problem I, in WILLIAMSON, S. J., HOKE, M., STROINK, G., and KOTANI, M. (Eds.) 'Advances in biomagnetism' (Plenum, New York) pp. 587–590
CROWLEY, C. W., GREENBLATT, R. E., and KHALIL, I. (1989): 'Minimum norm estimation of current distributions in realistic geometries' *Ibid.*, pp. 603–606
CUFFIN, B. N., and COHEN, D. (1977): 'Magnetic fields of a dipole in special volume conductor shapes,' *IEEE Trans.*, **BME-24**, pp. 372–381
DALLAS, W. J. (1985): 'Fourier space solution to the magnetostatic imaging problem,' *Appl. Opt.*, **24**, pp. 4543–4546
DE MUNCK, J. C., HÄMÄLÄINEN, M. S., and PETERS, M. J. (1991): 'The use of the asymptotic expansion to speed up the computation of a series of spherical harmonics,' *Clin. Phys. Physiol. Meas.*, **12(Suppl. A)**, pp. 83–87
GOLUB, G., HEATH, M., and WAHBA, C. (1979): 'Generalized cross-validation as a method for choosing a good ridge parameter,' *Technometrics*, **21**, pp. 215–223
HÄMÄLÄINEN, M. S. and ILMONIEMI, R. J. (1984): 'Interpreting measured magnetic fields of the brain: estimates of current distributions.' Technical Report TKK-F-A559, Helsinki University of Technology
HÄMÄLÄINEN, M. S. (1989): 'A 24-channel planar gradiometer: System design and analysis of neuromagnetic data' *in* WILLIAMSON, S. J., HOKE, M., STROINK, G. and KOTANI, M. (Eds.): 'Advances in biomagnetism' (Plenum, New York) pp. 639–644
HÄMÄLÄINEN, M. S., HARI, R., ILMONIEMI, R., KNUUTILA, J., and LOUNASMAA, O. V. (1993): 'Magnetoencephalography—theory, instrumentation, and applications to noninvasive studies of the working human brain,' *Rev. Mod. Phys.*, **65**, pp. 413–497
ILMONIEMI, R. J., and NUMMINEN, J. K. (1992): 'Synthetic magnetometer channels for standard representation of data' *in* HOKE, M., ERNÉ, S. N., OKADA, Y. C. and ROMANI, G. L. (Eds.): 'Biomagnetism 91: clinical aspects' (Elsevier, Amsterdam) pp. 793–796
ILMONIEMI, R. J., HÄMÄLÄINEN, M. S. and KNUUTILA, J. (1985): 'The forward and inverse problems in the spherical model' *in* WEINBERG, H., STROINK, G. and KATILA, T. (Eds.): 'Biomagnetism: applications & theory' (Pergamon Press, New York) pp. 278–282
IOANNIDES, A., BOLTON, J. and CLARKE, C. (1990): 'Continuous probabilistic solutions to the biomagnetic inverse problem,' *Inverse Probl.*
JEFFS, B., LEAHY, R., and SINGH, M. (1987): 'An evaluation of methods for neuromagnetic image reconstruction,' *IEEE Trans.*, **BME-34**, pp. 713–723
KAJOLA, M., AHLFORS, S., EHNHOLM, G. J., HÄLLSTRÖM, J., HÄMÄLÄINEN, M. S., ILMONIEMI, R. J., KIVIRANTA, M., KNUUTILA, J., LOUNASMAA, O. V., TESCHE, C. D. and VILKMAN, V. (1989): 'A 24-channel magnetometer for brain research' *in* WILLIAMSON, S. J., HOKE, M., STROINK, G. and KOTANI, M. (Eds.): 'Advances in biomagnetism' (Plenum, New York) pp. 673–676
KULLMANN, W. H., JANDT, K. D., REHM, K., SCHLITT, H. A., DALLAS, W. J. and SMITH, W. E. (1989): 'A linear estimation approach to biomagnetic imaging' *ibid.*, pp. 571–574
MALMIVUO, J. (1976): 'On the detection of the magnetic heart vector—an application of the reciprocity theorem'. PhD Thesis, Acta Polytechnica Scandinavica, Electrical Engineering Series 39, Finnish Academy of Technical Sciences, Helsinki.
MCLAIN, D. H. (1974): 'Drawing contours from arbitrary data points,' *Comput. J.*, **17**, pp. 318–324
NENONEN, J., HÄMÄLÄINEN, M., and ILMONIEMI, R. (1994): 'Minimum-norm estimation in a boundary element torso model,' *Med. & Biol. Eng. & Comput.*, 1994, **32**, (1) 43–49.
PLONSEY, R. (1969): 'Bioelectric phenomena' (McGraw-Hill, New York) p. 212
SARVAS, J. (1987): 'Basic mathematical and electromagnetic concepts of the biomagnetic inverse problem,' *Phys. Med. Biol.*, **32**, pp. 11–22
SINGH, M., DORIA, D., HENDERSON, V. W., HUTH, G. C. and BEATTY, J. (1984): 'Reconstruction of images from neuromagnetic fields,' *IEEE Trans.*, **NS-31**, pp. 585–589
SMITH, W. E., DALLAS, W. J., KULLMAN, W. H. and SCHLITT, H. A. (1990): 'Linear estimation theory applied to the reconstruction of a 3-D vector current distribution,' *Appl. Opt.*, **29**, pp. 658–667
TRIPP, J. H. (1983): 'Physical concepts and mathematical models' *in* WILLAMSON, S. J., ROMANI, G.-L., KAUFMAN, L. and MODENA, I. (Eds.): 'Biomagnetism: an interdisciplinary approach' (Plenum Press, New York) pp. 101–139
WILLIAMSON, S. J. and KAUFMAN, L. (1981): 'Biomagnetism,' *J. Magn. Magn. Mat.*, **22**, pp. 129–201

Appendix

This Appendix describes in detail a fast method for computing the dot product of magnetic lead fields in a spherically symmetric conductor earlier outlined by De Munck *et al.* (DE MUNCK *et al.*, 1991). The method is about four orders of magnitude faster than standard numerical integration techniques previously applied.

The magnetic scalar potential outside a sphere containing the conducting source region can be expressed as a series expansion in spherical harmonics:

$$\phi_m(\boldsymbol{r}') = \sum_{n=1}^{\infty} \sum_{m=0}^{n} (r')^{-n-1}[a^e_{nm} Y^e_{nm}(\theta', \varphi') + a^o_{nm} Y^o_{nm}(\theta', \varphi')] \tag{15}$$

where

$$Y^e_{nm} = P_{nm}(\cos\theta)\cos m\varphi \quad \text{and} \quad Y^o_{nm} = P_{nm}(\cos\theta)\sin m\varphi \tag{16}$$

are the even and odd terms, respectively. Here, $P_{nm}(\cos\theta)$ denote the associated Legendre polynomials of the first kind.

The magnetic field outside the conductor is obtained by taking the gradient of eqn. 15, $\boldsymbol{B} = -\mu_0 \nabla' \phi_m$, where μ_0 is the permeability of vacuum and ∇' denotes differentiation with respect to the primed co-ordinates.

The coefficients of the series expansion (eqn. 15) for a dipole source in a spherically symmetric conductor are

$$a^{e,o}_{nm} = \frac{r^n}{(n+1)(2n+1)} \| Y_{nm} \|^{-2} \left[Q_\theta \frac{1}{\sin\theta} \frac{\partial}{\partial\varphi} - Q_\varphi \frac{\partial}{\partial\theta} \right] Y^{e,o}_{nm}(\theta, \varphi) \tag{17}$$

where r, θ and φ are the spherical co-ordinates of the dipole location, Q_θ and Q_φ are its two tangential components, and $\| Y_{nm} \|$ is the norm:

$$\| Y_{nm} \|^2 = \frac{4\pi}{(2n+1)(2-\delta_{0m})} \frac{(n+m)!}{(n-m)!} \tag{18}$$

Our task is to compute the integral

$$\langle L_1, L_2 \rangle = \int \boldsymbol{L}_1(\boldsymbol{r}) \cdot \boldsymbol{L}_2(\boldsymbol{r}) dv \tag{19}$$

where $\boldsymbol{L}_1$ and $\boldsymbol{L}_2$ are the lead fields of point magnetometers at $\boldsymbol{r}_1$ and $\boldsymbol{r}_2$. Their sensitivity directions are denoted by the unit vectors $\boldsymbol{n}_1$ and $\boldsymbol{n}_2$, respectively.

From the definition of the lead field

$$\boldsymbol{L}_k(\boldsymbol{r}) = [\boldsymbol{B}^\theta(\boldsymbol{r}_k, \boldsymbol{r}) \cdot \boldsymbol{n}_k / Q_\theta]\boldsymbol{e}_\theta + [\boldsymbol{B}^\varphi(\boldsymbol{r}_k, \boldsymbol{r}) \cdot \boldsymbol{n}_k / Q_\varphi]\boldsymbol{e}_\varphi \tag{20}$$

where $\boldsymbol{B}^q(\boldsymbol{r}_k, \boldsymbol{r})$ denotes the magnetic field at $\boldsymbol{r}_k$ due to a dipole $\boldsymbol{Q} = Q_q \boldsymbol{e}_q$ at $\boldsymbol{r}$.

We can now express eqn. 19 in terms of the scalar potential:

$$\langle L_1, L_2 \rangle = \mu_0^2 \int (\boldsymbol{n}_1 \cdot \nabla_1)(\boldsymbol{n}_2 \cdot \nabla_2)[\phi^\theta_m(\boldsymbol{r}_1, \boldsymbol{r})\phi^\theta_m(\boldsymbol{r}_2, \boldsymbol{r}) + \phi^\varphi_m(\boldsymbol{r}_1, \boldsymbol{r})\phi^\varphi_m(\boldsymbol{r}_2, \boldsymbol{r})] dv \tag{21}$$

where ∇_k denotes differentiation with respect to $\boldsymbol{r}_k$ and $\phi_m^q(\boldsymbol{r}_k, \boldsymbol{r})$ is the scalar potential at $\boldsymbol{r}_k$, obtained by setting $Q_q = 1$.

We now exchange the order of integration and differentiation, so that

$$\langle L_1, L_2 \rangle = \mu_0^2(\boldsymbol{n}_1 \cdot \nabla_1)(\boldsymbol{n}_2 \cdot \nabla_2)\Pi^m(\boldsymbol{r}_1, \boldsymbol{r}_2) \tag{22}$$

where

$$\Pi^m(\boldsymbol{r}_1, \boldsymbol{r}_2) = \int [\phi_m^\theta(\boldsymbol{r}_1, \boldsymbol{r})\phi_m^\theta(\boldsymbol{r}_2, \boldsymbol{r}) + \phi_m^\varphi(\boldsymbol{r}_1, \boldsymbol{r})\phi_m^\varphi(\boldsymbol{r}_2, \boldsymbol{r})] f(r) dv \tag{23}$$

and $f(r)$ is a radial weighting function. When integrating uniformly over a sphere, we take $f(r) = 1$ for $r < r_0$, whereas, for a spherical shell, $f(r) = \delta(r - r_0)$, where $\delta(r)$ is the Dirac delta function.

With eqns. 15 and 17, eqn. 23 becomes

$$\Pi^m(\boldsymbol{r}_1, \boldsymbol{r}_2) = \sum_{nn'\alpha\alpha'} \left\{ r_1^{-n-1} r_2^{-n'-1} \int_0^\infty f(r) r^{n+n'+2}\, dr \times \sum_{mm'} \left[\frac{\| Y_{nm} \|^{-2} \| Y_{n'm'} \|^{-2}}{(n+1)(2n+1)(n'+1)(2n'+1)} \times Y_{nm}^{\alpha}(\theta_1, \varphi_1) Y_{n'm'}^{\alpha'}(\theta_2, \varphi_2) \times \int_0^{2\pi} \int_0^{\pi} I_{nmn'm'}^{\alpha\alpha'} \sin\theta\, d\theta\, d\varphi \right] \right\} \tag{24}$$

where $\alpha, \alpha' = e, o$ and

$$I_{nmn'm'}^{\alpha\alpha'} = \frac{1}{\sin^2\theta} \frac{\partial}{\partial\varphi} Y_{nm}^{\alpha}(\theta, \varphi) \frac{\partial}{\partial\varphi} Y_{n'm'}^{\alpha'}(\theta, \varphi) + \frac{\partial}{\partial\theta} Y_{nm}^{\alpha}(\theta, \varphi) \frac{\partial}{\partial\theta} Y_{n'm'}^{\alpha'}(\theta, \varphi) \tag{25}$$

The integration over φ yields $2\pi\delta_{\alpha\alpha'}\delta_{mm'}/(2 - \delta_{0m})$. The remaining integral over θ can be evaluated using the identity

$$\int_0^\pi \left[\frac{m^2}{\sin^2\theta} P_{nm}(\cos\theta) P_{n'm}(\cos\theta) + \sin^2\theta P'_{nm}(\cos\theta) P'_{n'm}(\cos\theta) \right] \sin\theta\, d\theta = \delta_{nn'} \frac{2n(n+1)}{2n+1} \frac{(n+m)!}{(n-m)!} \tag{26}$$

Thus

$$\int_0^{2\pi} \int_0^\pi I_{nmn'm'}^{\alpha\alpha'} \sin\theta\, d\theta\, d\varphi = \delta_{nn'}\delta_{mm'} n(n+1) \| Y_{nm} \|^2 \tag{27}$$

and

$$\Pi^m(\boldsymbol{r}_1, \boldsymbol{r}_2) = \frac{1}{4\pi} \sum_n \left\{ \frac{n}{(n+1)(2n+1)} (r_1 r_2)^{-n-1} \times \int_0^r f(r) r^{2n+2}\, dr \sum_m (2 - \delta_{0m}) \frac{(n-m)!}{(n+m)!} \times [Y_{nm}^e(\theta_1, \varphi_1) Y_{nm}^e(\theta_2, \varphi_2) + Y_{nm}^o(\theta_1, \varphi_1) Y_{nm}^o(\theta_2, \varphi_2)] \right\} \tag{28}$$

Finally, using the addition theorem for spherical harmonics on the second line of eqn. 28, we arrive at

$$\Pi^m(\boldsymbol{r}_1, \boldsymbol{r}_2) = \frac{1}{4\pi} \sum_{n=0}^{\infty} \left[\frac{1}{(r_1 r_2)^{n+1}} \frac{n}{(n+1)(2n+1)} \times P_n(\cos\gamma) \int_0^\infty r^{2n+2} f(r) dr \right] \tag{29}$$

where

$$\cos\gamma = \cos\theta_1 \cos\theta_2 + \sin\theta_1 \sin\theta_2 \cos(\varphi_1 - \varphi_2) = \boldsymbol{r}_1 \cdot \boldsymbol{r}_2 / r_1 r_2 \tag{30}$$

If the integration goes over one spherical shell only, $f(r) = \delta(r - r_0)$, and we obtain

$$\Pi^m(\boldsymbol{r}_1, \boldsymbol{r}_2) = \frac{1}{4\pi} \sum_{n=1}^{\infty} \beta^{n+1} \frac{n}{(n+1)(2n+1)} P_n(\cos\gamma) \tag{31}$$

with $\beta = r_0^2 / r_1 r_2$.

To find the lead-field products, we will still have to differentiate eqn. 31 according to eqn. 22 and multiply with μ_0^2. With $\boldsymbol{r}_k = r_k(c_{k1}\boldsymbol{e}_x + c_{k2}\boldsymbol{e}_y + c_{k3}\boldsymbol{e}_z)$, we obtain

$$\Pi_{jk}^m \equiv \frac{\partial^2 \Pi^m}{\partial c_{1j} \partial c_{2k}} = \sum_{p=1}^{4} q_p \Sigma_p \tag{32}$$

where

$$\begin{aligned} q_1 &= c_{1j} c_{2k} & \Sigma_1 &= \sum_{n=1}^{\infty} \frac{n(n+1)}{2n+1} \beta^{n+1} P_n(\cos\gamma) \\ q_2 &= 2c_{1j}c_{2k}\cos\gamma - c_{1j}c_{1k} - c_{2k}c_{2j} & \Sigma_2 &= \sum_{n=1}^{\infty} \frac{n}{2n+1} \beta^{n+1} P'_n(\cos\gamma) \\ q_3 &= q_2 + \delta_{jk} - c_{1j}c_{2k}\cos\gamma & \Sigma_3 &= \sum_{n=1}^{\infty} \frac{n}{(n+1)(2n+1)} \beta^{n+1} P'_n(\cos\gamma) \\ q_4 &= (c_{2j} - c_{1j}\cos\gamma)(c_{1k} - c_{2k}\cos\gamma) & \Sigma_4 &= \sum_{n=1}^{\infty} \frac{n}{(n+1)(2n+1)} \beta^{n+1} P''_n(\cos\gamma) \end{aligned} \tag{33}$$

The primes denote the derivatives of the Legendre polynomials with respect to the argument $\cos\gamma$. The lead-field product can be now combined from the partial derivatives:

$$\langle L_1, L_2 \rangle = \frac{\mu_0^2}{r_1 r_2} \sum_{j,k=1}^{3} n_{1j} n_{2k} \Pi_{jk}^m \tag{34}$$

where we have used $\boldsymbol{n}_k = (n_{k1}\boldsymbol{e}_x + n_{k2}\boldsymbol{e}_y + n_{k3}\boldsymbol{e}_z)$ as before.

Authors' biographies

Matti Hämäläinen was born in 1958. He joined the neuromagnetism group at the Low Temperature Laboratory of Helsinki University of Technology in 1981, and received his MSc in Physics from there in 1983. His PhD thesis in 1987 discussed the neuromagnetic inverse problem and the statistical evaluation of MEG data. Recently he has been developing source analysis methods and software for a whole-cortex neuromagnetometer system.

Risto Ilmoniemi was born in 1954. He received his MSc and PhD in Physics from the Helsinki University of Technology in 1981 and 1985, respectively. He joined the Low Temperature Laboratory in 1978. From 1985 until 1987 he worked at the Neuromagnetism laboratory of New York University. His research interests at the Low Temperature Laboratory include multichannel magnetometers and electrode arrays, the biomagnetic inverse problem, evoked magnetic fields, spontaneous brain activity and computer-aided education.